Real-time computation of the TMS-induced electric field in a realistic head model

Matti Stenroos* and Lari Koponen

Aalto University School of Science
Department of Neuroscience and Biomedical Engineering
February 11, 2019

Abstract

Background: Transcranial magnetic stimulation (TMS) is often targeted using a model of TMS-induced electric field (E). In such navigated TMS, the E-field models have been based on spherical approximation of the head. Such models omit the effects of cerebrospinal fluid (CSF) on the E-field, leading to potentially large errors in the computed field. So far, realistic models have been too slow for interactive TMS navigation.

Objective: We present computational methods that enable real-time solving of the E-field in a realistic head model that contains the CSF.

Methods: Using reciprocity and Geselowitz integral equation, we separate the computations to coil-dependent and -independent parts. For the coil-dependent part of Geselowitz integrals, we present a fast numerical quadrature. Further, we present a moment-matching approach for optimizing dipole-based coil models. We verify the new methods using simulations in a realistic head model that contains the brain, CSF, skull, and scalp.

Results: The new quadrature introduces a relative error of 1.1%. The total error of the quadrature and coil model was 1.43% and 1.15% for coils with 38 and 76 dipoles, respectively. The difference between our head model and a simpler realistic model that omits the CSF was 29%. Using a standard PC and a 38-dipole coil, our solver computed the E-field in 84 coil positions per second in 20000 points on the cortex.

Conclusion: The presented methods enable real-time solving of the TMS-induced E-field in a realistic head model that contains the CSF. The new methodology allows more accurate targeting and precise adjustment of intensity during experimental or clinical TMS mapping.

Keywords transcranial magnetic stimulation (TMS); navigated transcranial magnetic stimulation; electric field calculation; coil model; volume conductor model

*Corresponding author, matti.stenroos@aalto.fi

1 Introduction

In transcranial magnetic stimulation (TMS) [1], a brief current pulse in a coil gives rise to a time-varying magnetic field that causes an electric field (E-field), and the E-field stimulates the brain. The E-field consists of two parts: the primary E-field $\vec{E}_{\mathrm{p}}$ induced by the changing magnetic field causes a current distribution in the head, and this current is affected by changes of electric conductivity, leading to charge buildup at conductivity interfaces. These charges give rise to a secondary electric field $\vec{E}_{\mathrm{s}}$, the total E-field thus being $\vec{E}_{\mathrm{p}} + \vec{E}_{\mathrm{s}}$.

In navigated TMS, the stimulation is targeted and its intensity is set using a model of TMS-induced E-field. For this, we need a volume conductor model (VCM) that characterizes the conductivity distribution of the head. While simulation and offline TMS studies use realistically-shaped highly detailed VCMs [2, 3, 4, 5], in experimental navigated TMS the head has so far been modeled as a spherically symmetric conductor that is fitted to approximate either the shape of the skull under the coil or the whole skull. Spherical models omit the effects of well-conducting cerebrospinal fluid (CSF) [2, 6] and may fail in approximating the effects of skull at regions of changing skull curvature [7].

To optimally benefit from the E-field model in navigation, the E-field should be computed in near real time, so that the operator can see the estimated field pattern while moving the TMS coil. With tools used for solving realistic VCMs in, for example, [4, 5] and approaches proposed recently in [8, 9], computation of the E-field takes of the order of tens of seconds to minutes for one coil position.

In this paper, we present and benchmark computational methods that allow fast solving the E-field in a realistic VCM, tens of coil positions per second. Our approach is based on the reciprocity relation [10, 11] and surface-integral solution of the magnetic field in a VCM [12]. The same idea has earlier been applied in, for example, [7]. Here, we present a formulation optimized for repeated computations, and speed up the computations with two novel techniques: a simple-but-adequate numerical quadrature for surface integrals and a moment-matching approach to optimize the coil model for rapid computations. Together these enable the real-time computation of E-field in a realistic VCM. The fast quadrature is applicable to any reciprocity-based approach in isotropic VCMs, and the coil-modeling technique can be used in any computational environment that models coils using a set of dipoles or that solves the E-field reciprocally.

2 Methods

Reciprocity relation Let there be a system of conductors. Let primary current distribution $\vec{J}_1^{\mathrm{p}}$ give rise to electric field $\vec{E}_1$. Correspondingly, $\vec{J}_2^{\mathrm{p}}$ gives rise to $\vec{E}_2$. Then, assuming the head electrically resistive and small compared to the wavelength of electromagnetic waves, we get the reciprocity relation [10]

$$\int\limits_{\text{all } \vec{J}_1^{\mathrm{p}}} \vec{J}_1^{\mathrm{p}} \cdot \vec{E}_2 \, dV = \int\limits_{\text{all } \vec{J}_2^{\mathrm{p}}} \vec{J}_2^{\mathrm{p}} \cdot \vec{E}_1 \, dV. \tag{1}$$

Letting $\vec{J}_1^{\mathrm{p}}$ be a dipolar current element $\vec{Q}$ at $\vec{r}_{\mathrm{Q}}$ and $\vec{J}_2^{\mathrm{p}}$ a current loop (coil) with current I flowing in a thin wire c, we get [11]

$$\vec{Q} \cdot \vec{E}(\vec{r}_{\mathrm{Q}}) = -\frac{dI}{dt} \int_S \vec{B} \cdot \vec{dS}, \tag{2}$$

where $\vec{E}$ is the electric field generated by dI/dt, $\vec{B}$ is the magnetic field produced by $\vec{Q}$, and $c = \partial S$ is the boundary of S. Setting an unit-current dipole $\hat{Q}$ to $\vec{r}_{\mathrm{Q}}$ and computing its magnetic flux through the coil, we get the corresponding component of $\vec{E}$ in $\vec{r}_{\mathrm{Q}}$.

Forward problem for primary current distribution in the head Consider a primary current distribution in a piece-wise homogeneous isotropic volume conductor that has K boundary surfaces separating the compartments of different conductivities. Let superscripts in italics label boundary surfaces. The magnetic field in or outside of the conductor is [12]

$$\vec{B}(\vec{r}) = \vec{B}^{\mathrm{p}}(\vec{r}) + \overbrace{\frac{\mu_0}{4\pi} \sum_{k=1}^{K} (\sigma_+^k - \sigma_-^k) \int_{S^k} \phi(\vec{r}\,') \, \vec{dS}' \times \frac{(\vec{r} - \vec{r}\,')}{|\vec{r} - \vec{r}\,'|^3}}^{\vec{B}^{\mathrm{s}}(\vec{r})}, \tag{3}$$

where σ_+^k and σ_-^k are the conductivities outside and inside of boundary k, $\vec{B}^{\mathrm{p}}$ is the primary magnetic field due to $\vec{J}^{\mathrm{p}}$, ϕ is the electric potential generated by the charge density associated with the $\vec{J}^{\mathrm{p}}$, and $\vec{B}^{\mathrm{s}}$ is the secondary magnetic field due to conductivity inhomogeneities in the head.

Now discretize the conductivity boundaries into a set of vertices and triangular elements, and express the boundary potentials ϕ^k using basis functions: $\phi^k(\vec{r}) = \sum_{j=1}^{N^k} \varphi_j^k \psi_j^k(\vec{r})$, where φ_j^k is the potential in the vertex j of boundary k (target vertex), and $\psi_j^k(\vec{r})$ is a linear basis function that is spanned on the member triangles of the target vertex and gets value of 1 in the target vertex and value of 0 in the other vertices[1]. We get

$$\vec{B}^{\mathrm{s}}(\vec{r}) \approx \frac{\mu_0}{4\pi} \sum_{k=1}^{K} (\sigma_+^k - \sigma_-^k) \sum_{j=1}^{N^k} \varphi_j^k \overbrace{\int_{\mathrm{Ne}_j^k} \psi_j^k(\vec{r}\,') \, \vec{dS}' \times \frac{(\vec{r} - \vec{r}\,')}{|\vec{r} - \vec{r}\,'|^3}}^{\vec{\beta}_j^k(\vec{r})}, \tag{4}$$

[1] Here we use triangle meshes and linear basis functions, but the approach is straightforward to generalize to other element types.

where $\vec{\beta}_j^k(\vec{r})$ is the integral that needs to be computed repeatedly for all elements and field points, when the TMS coil is moved.

To compute the magnetic flux through a coil, we need to set up a numerical integration scheme. For this purpose, we compute the normal component $B_n = \vec{B}(\vec{r}) \cdot \vec{n}(\vec{r})$ in N^{c} quadrature points in the coil. For any source distribution, we then get the matrix form

$$\int_S \vec{B} \cdot \vec{dS} \approx \mathbf{w}^{\mathrm{T}}\mathbf{B} = \mathbf{w}^{\mathrm{T}}(\mathbf{B}^{\mathrm{p}} + \mathbf{D}\boldsymbol{\phi}), \tag{5}$$

where $\mathbf{w}^{\mathrm{T}}$ $(1 \times N^{\mathrm{c}})$ contains coil quadrature weights, $\mathbf{B}^{\mathrm{p}}$ $(N^{\mathrm{c}} \times 1)$ contains $\vec{B}^{\mathrm{p}} \cdot \vec{n}$ in the quadrature points, $\mathbf{D}$ $(N^{\mathrm{c}} \times N^{\mathrm{v}})$ contains $\vec{\beta}_j^k \cdot \vec{n}$ for the coil quadrature points and all basis functions, and $\boldsymbol{\phi}$ $(N^{\mathrm{v}} \times 1)$ contains φ_j^k in all model vertices and all the remaining constants and material parameters of Eq. 4.

To compute TMS-induced $\vec{E}$ on the cortex using Eq. 2, we need to solve Eq. 5 for dipole sources placed all over the cortical region of interest (N^{ROI} dipoles). The accuracy and computational cost of the solution depend on:

1. the accuracy of the volume conductor model and $\boldsymbol{\phi}$; the discretization and number of vertices N^{v},
2. the method used for computing $\vec{\beta}_j^k$,
3. the accuracy and number of quadrature points N^{c} of the coil model, and
4. the extent and discretization density N^{ROI} of the ROI.

Potential $\boldsymbol{\phi}$ does not depend on the TMS coil. It can thus be computed in advance for the region of interest, using the desired level of detail and numerical approach. In this work, we focus on coil integrals, that is, points 2 and 3 of the above list.

2.1 Fast quadrature for computing secondary magnetic field

When accurately computing the secondary magnetic field $\vec{B}^{\mathrm{s}}$ using Eq. 5, we need to evaluate N^k surface integrals, each spanned in the neighborhood of one vertex. Typically the computation is carried out triangle-wise, using linear shape functions that have value of 1 in one vertex and value of 0 in the other vertices of the triangle. For these shape functions, we have a closed-form analytical solution of $\vec{\beta}_j^k$ [13]. In applications, where no real-time modeling is needed (for example, magnetoencephalography and magnetocardiography), that approach works excellently. For the real-time TMS approach it might, however, become a bottleneck, so we will apply numerical integration.

In numerical integration over a meshed surface, each element is typically represented by a set of quadrature points $\vec{q}_i$ and weights w_i: for one element, $\int \vec{f}(\vec{r})\, dS \approx \sum_i w_i \vec{f}(\vec{q}_i)$. With flat triangular elements, Gaussian quadrature with either 7 or 13 points per triangle

is a typical choice. As each vertex has on the average six member triangles, a 7-point quadrature would result in evaluating the integrand of $\vec{\beta}_j^k$ in approximately 42 points. Each triangle belonging to three vertices, the approximate number of quadrature points per vertex would then be 14. We will, however, take one step further and represent $\vec{\beta}_j^k(\vec{r})$ using only one quadrature point per vertex neighborhood.

Let vertex $\vec{r}_j^k$ have N member triangles T_i that have normal vectors $\vec{n}_i$ and areas A_i. The basis function ψ is then expressed using N shape functions s_i. For each $s_i(\vec{r})$, find its center of mass $\vec{c}_{T_i}$ and compute the dipole moment $\vec{m}_{T_i}$ of $s_i\vec{n}_i$. Then, to get the equivalent dipole for the whole $\psi_j^k(\vec{r})\vec{n}(\vec{r})$, compute the weighted center of mass $\vec{c}_j^k$ and the total dipole moment $\vec{m}_j^k$:

$$\vec{c}_j^k = \frac{1}{\sum_{i=1}^N A_i} \sum_{i=1}^N A_i \overbrace{\int_{T_i} s_i(\vec{r})\vec{r}\, dS \Big/ \int_{T_i} s_i(\vec{r})\, dS}^{\vec{c}_{T_i}} \tag{6}$$

$$\vec{m}_j^k = \sum_{i=1}^N \overbrace{\int_{T_i} s_i(\vec{r})\vec{n}_i\, dS}^{\vec{m}_{T_i}} = \frac{1}{3}\sum_{i=1}^N A_i\vec{n}_i. \tag{7}$$

Thus

$$\vec{\beta}_j^k(\vec{r}) = \int_{\mathrm{Ne}_j^k} \psi_j^k(\vec{r}')\, \vec{d}S' \times \frac{(\vec{r}-\vec{r}')}{|\vec{r}-\vec{r}'|^3} \approx \vec{m}_j^k \times \frac{(\vec{r}-\vec{c}_j^k)}{|\vec{r}-\vec{c}_j^k|^3}. \tag{8}$$

2.2 Coil model

To obtain the E-field, we numerically compute the integral on the right hand side of Eq. 2. The coil is represented as a set of (oriented) quadrature points as in the previous section. Or, thinking the other way, the current loops of the coil are represented as a set of magnetic dipoles (see, e.g., [14]). A set of dipoles that represents a TMS coil can be generated by discretizing the volume where the coil windings lie into smaller sub-volumes [14, 15, 7]; similar approaches are also used with permanent magnets [16]. As the TMS coil is relatively large and close to the head, this approach, however, requires a large number of dipoles for accurate representation of the windings. For example, in [14], the Magstim 70mm Double Coil (P/N 9925) whose windings span a volume of $176 \times 88 \times 7$ mm^3 was represented with 2712 dipoles in three identical layers. For real-time computation, we would prefer a much lower number of dipoles—of the order of at most one hundred.

Consider a coil as a magnetic dipole moment density distribution. Assuming unit current in the coil windings, the magnetic dipole moment density f at each point in space equals the number of turns surrounding that point. Such a distribution can be characterized by its geometric moments. Let us consider the case of a planar coil aligned with the xy plane; all magnetic dipoles thus point at $\pm\hat{z}$ direction. The geometric moment μ of the order

(n_x, n_y, n_z) is

$$\mu_{n_x,n_y,n_z} = \iiint_{V_{\text{coil}}} x^{n_x} y^{n_y} z^{n_z} \frac{f(x,y)}{h} \, \mathrm{d}x \, \mathrm{d}y \, \mathrm{d}z \tag{9}$$

where $f(x, y)$ counts the number of turns surrounding each location and h is the height of the windings. The calculation can be separated into two parts,

$$\mu_{n_x,n_y} = \iint_{A_{\text{coil}}} x^{n_x} y^{n_y} f(x,y) \, \mathrm{d}x \, \mathrm{d}y \tag{10}$$

$$\mu_{n_z} = \int_{h_{\text{coil}}} \frac{z^{n_z}}{h} \, \mathrm{d}z \; . \tag{11}$$

Consider first the simpler z direction. The n_z-order moment of a discrete set of dipoles is

$$\mu'_{n_z} = \sum_i z_i^{n_z} w_i \; , \tag{12}$$

where w_i is the weight of each dipole; negative w_i means that the ith dipole points $-\hat{z}$ direction. If we place the coil symmetrically around the origin, odd terms vanish, and with I dipoles we get a system of equations

$$\forall n_z \in \{0, 2, \ldots, 2I\} : \mu_{n_z} = \mu'_{n_z} \; . \tag{13}$$

For the x and y directions the (n_x, n_y)-order moment of a discrete set of dipoles is

$$\mu'_{n_x,n_y} = \sum_j x_j^{n_x} y_j^{n_y} w_j . \tag{14}$$

If we match all moments μ'_{n_x,n_y} and μ_{n_x,n_y} up to a degree $n_x + n_y = N$, we obtain a translation invariant solution. Thus, we can consider the two wings separately and solve the problem for one set of circular loops around the origin.

Consider a circular loop, radius r, at origin. The (n_x, n_y)-order moment for the corresponding $f(x, y)$ is

$$\mu_{n_x,n_y} = \int_{-r}^{r} \int_{-\sqrt{r^2-x^2}}^{\sqrt{r^2-x^2}} x^{n_x} y^{n_y} \, \mathrm{d}y \, \mathrm{d}x \; , \tag{15}$$

for which a closed-form solution can be obtained (e.g., using a computer software for symbolic mathematics). Place n dipoles per ring in 0–2 rings so that there is symmetry along at least one axis and n-fold rotational symmetry. In addition, we allow a point at the origin—see Figure 1 for an example placement. For sufficient n, the ring-like structure will, due to symmetry, always match either none or all moments of degree N, which reduces the number of unique equations from $N(N + 1)/2$ to N.

2.3 Simulations

We tested the effects of β quadrature and our coil model approximation on cortical E field using computer simulations in a realistic head model. Our head model was

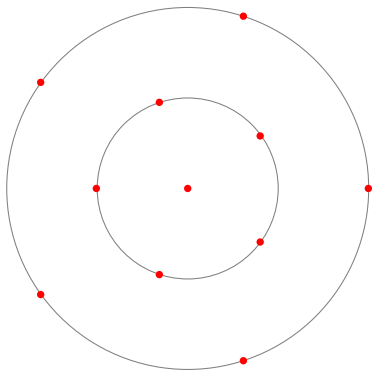

Figure 1: *An example dipole placement with one dipole at the origin, and two rings of five dipoles. The outermost ring can have two possible orientations; the shown one, i.e., not aligned with the innermost ring, can solve all moments up to the degree of 6.*

built on the anatomical model of the sample data set of SimNIBS software [17] and the coil model based on the description of the Magstim 70mm Double Coil in [14]. Head model computations and coil comparisons were carried out in Matlab (version R2017b, www.mathworks.com), while speed tests for the E-field calculation were done both in Matlab and in C language (gcc 5.4.0). All computations were carried out on standard desktop computers running Ubuntu 16.04.

For head model, we extracted the meshes for the outer boundary of the brain and cerebellum, inner and outer skull boundaries, and outer scalp boundary and resampled them using iso2mesh toolbox [18] and in-house tools to triangle side-lengths (TSL) of 4, 5, 5, 6, and 7 mm, respectively, resulting in a total number of vertices $N^{\mathrm{v}} = 21053$. The model geometry is illustrated in Figure 2. Using these meshes as conductivity boundaries, we built a four-compartment Galerkin boundary-element model [19, 20] for electric potential. Next, we extracted the boundary of white and gray matter, resampled it to the TSL of 3 mm (number of vertices $N^{\mathrm{b}} = 20324$), placed normally-oriented unit-current dipoles $\hat{Q}$ to the vertices, and computed boundary potentials ϕ for all these dipoles. For further detail on model construction and verification, please see [20].

For reference coil model, we divided the example coil into 1 mm^3 cubic voxels, each represented by one dipole. Current was assumed to be spread evenly within the wires, and the weight of the dipole was set to the mean value of f in the voxel. This discretization approach, illustrated in Figure 3, resulted in a total of 85288 dipoles in 7 uniformly spaced layers. In test coil models, we had 1–3 layers with 2–42 dipoles in each, resulting in altogether 27 test coils containing 2–126 dipoles. In addition, we tested the Thielscher–Kammer (TK) coil model [14] that has 2712 dipoles.

The coil was placed tangentially over the scalp in 251 separate positions around the head, following a 256-electrode EEG electrode layout. The coil was oriented so that the primary E-field would be approximately normal to the cortex in a region under the coil center. For

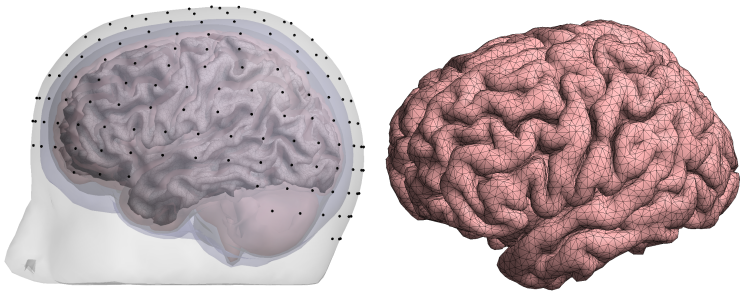

Figure 2: *Computation geometry. The plot on the left shows all conductivity boundaries and also the field computation surface. The plot on the right shows the boundary between the brain and CSF. The locations of the stimulation coil (center of the coil projected to scalp) are shown with black dots in the left-side plot.*

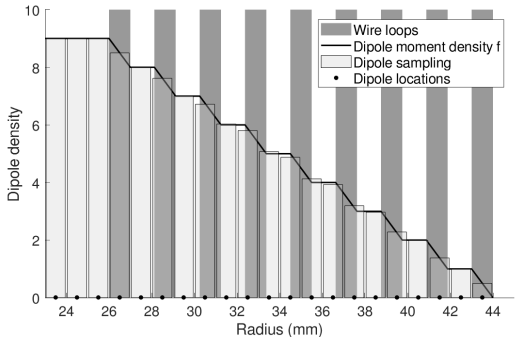

Figure 3: *Discretization of our reference coil into a set of magnetic dipoles: The locations of wire loops are shown with dark gray rectangles, and dipole moment density f is plotted with a black line. The sampling regions and equivalent value of f for each dipole is shown with light gray rectangles, and the dipole locations are shown with black dots.*

each coil position, we computed the E-field across the whole cortex using different coil models and both accurate and approximated β integrals. Our main comparison metric was the maximum of the normalised error in the normal component of the E-field in the cortex, maxRE:

$$\mathrm{maxRE} = \frac{\max|\mathbf{E}^{\mathrm{test}} - \mathbf{E}^{\mathrm{ref}}|}{\max|\mathbf{E}^{\mathrm{ref}}|}, \tag{16}$$

where $\mathbf{E}$ contains $\vec{E} \cdot \vec{n}$ in all 20324 vertices of the cortical surface and 'ref' and 'test' refer to reference and test models. In addition, to assess the similarity of E-field shapes, we computed correlation coefficients CC between $\mathbf{E}^{\mathrm{ref}}$ and $\mathbf{E}^{\mathrm{test}}$.

For selected coil models, we performed speed testing. We solved the normal component of $\vec{E}$ in either the whole brain (number of field points N^{b}) or in a region-of-interest around the projected coil center (mean $N^{\mathrm{ROI}} = 1805$, cortical surface area 117 cm^2,

radius approximately 6 cm, each coil location having its own ROI). Potential ϕ was precomputed for all N^{b} oriented sources on the cortex, resulting in $(N^{\mathrm{v}} \times N^{\mathrm{b}})$ matrix $\mathbf{\Phi}$. For each coil position, following computations were done:

- Build $\mathbf{D}$ and compute $\mathbf{d} = \mathbf{w}^{\mathrm{T}}\mathbf{D}$, resulting in a $(1 \times N^{\mathrm{v}})$ vector.
- Build $\mathbf{B}^{\mathrm{p}}$ for all field points and compute $\mathbf{w}^{\mathrm{T}}\mathbf{B}^{\mathrm{p}}$, resulting in a $(1 \times N^{\mathrm{ROI}})$ vector.
- Compute $\mathbf{d}\tilde{\mathbf{\Phi}}$, where $\tilde{\mathbf{\Phi}}$ is either the full $(N^{\mathrm{v}} \times N^{\mathrm{b}})$ matrix $\mathbf{\Phi}$ or N^{ROI} columns of it.

The benchmarking computer had a 4-core processor (Intel Xeon E3-1230 v5) and a consumer-level graphics card (Nvidia GeForce GTX 1060). The Matlab implementation used the GPU for computing the multiplication $\mathbf{d}\tilde{\mathbf{\Phi}}$, while the C implementation used only the CPU.

3 Results

3.1 Coil model parameters

We solved the z-coordinates of dipole layers for an origin-centered planar coil of thickness d as described in Eqs. 11–13. The solving of Eq. 13 was done for one to four layers I using Mathematica software (version 10.3.0, www.wolfram.com). This resulted in optimal layer positions and weights shown in Table 1. The layers are placed less densely in the center and more densely towards the coil boundaries, while the central layers have higher weights than the ones closer to the boundaries.

Then, we sought the optimal distribution of dipoles, looking for the minimum number of dipoles that produces the exact match of moments μ'_{n_x,n_y} and μ_{n_x,n_y} up to a degree $n_x + n_y = N$ for a system of circular rings. A systematic search through all possible sets of dipoles for $N \leq 9$ gave us the dipole placement rules shown in Table 2. Unlike with z direction, the weights and radii cannot be given in closed form for an arbitrary coil. Thus, we continued by fitting the radii and weights for one wing of our example coil, where each wire loop shown in Figure 3 was further represented with 10 equally spaced thin circular loops of Eq. 15, and the system of polynomial equations was solved using Mathematica. At the end we then had 9 sets of dipoles in the central plane of the coil. With these, we implemented the whole coil using 1, 2, or 3 layers, resulting in 27 test coil models.

3.2 Coil model comparisons

We evaluated the accuracy of the β integral approximation and the coil models by comparing the cortical E-fields to those obtained with the reference model. As reference, we

Table 1: *Optimal layers (z_i) and their weights (w_i) for discretisation of a planar coil with thickness d, centred around origin.*

I	z_i/d				w_i			
1	0				1			
2	-0.2887	0.2887			0.5	0.5		
3	-0.3873	0	0.3873		0.2778	0.4444	0.2778	
4	-0.4306	-0.1700	0.1700	0.4306	0.1739	0.3261	0.3261	0.1739

Table 2: *Dipole placement rules for minimum number of dipoles to match all moments up to a degree of N of a system of planar circular disks. The dipoles in each ring r_i have equal weights and equidistant spacing of $360°/n_{r_i}$, and the two rings of dipoles for the last four rows have an offset of $180°/n_{r_i}$. Subscript o indicates the origin.*

N	1	2	3	4	5	6	7	8	9
n_{o}	1			1	1	1	1	1	1
n_{r_1}		3	4	5	6	5	6	9	10
n_{r_2}						5	6	9	10

used accurate β integrals and our reference coil model that has 85288 dipoles. For all test models and accurate and approximate β, we computed the maxRE and CC across the cortex and took the root-mean-square value across coil locations ($\mathrm{maxRE_{rms}}$, $\mathrm{CC_{rms}}$). For all coils mentioned in the text, except the 14-dipole coil, the $\mathrm{CC_{rms}}$ was larger than 99.99%.

First, we evaluated the error due to the fast numerical approximation of β integrals (Eq. 8). Comparing the reference E-field with that obtained with the reference coil but approximate β integrals resulted in the $\mathrm{maxRE_{rms}}$ of 1.08%. In test coils, the increase of error due to β approximation was between 0.1% and 0.8%, overall increasing with the number of dipoles (see Fig. 4a).

Then, we evaluated the total error (β approximation + coil model) of all test coil models, The results are shown in Fig. 4b. With respect to the number of dipoles, the single-layer coil with 38 dipoles performs best, with the total $\mathrm{maxRE_{rms}}$ of 1.43%. The number of layers in the coil model has rather small effect—computational resources are best spent on single-layer coils. With accurate and approximated β integrals, the TK coil model with 2712 dipoles had the $\mathrm{maxRE_{rms}}$ of 4.3% and 4.7%, respectively.

Our head model had four compartments, the brain + cerebellum, CSF, skull, and scalp. We constructed also three- and single-shell models and computed corresponding cortical E-fields; the difference between the four-compartment reference model and the three- and single-shell models, evaluated with the $\mathrm{maxRE_{rms}}$, was 29% and 31%, respectively. The corresponding CCs were 98.45% and 98.16%. These differences are much larger than the errors due to β and coil approximations.

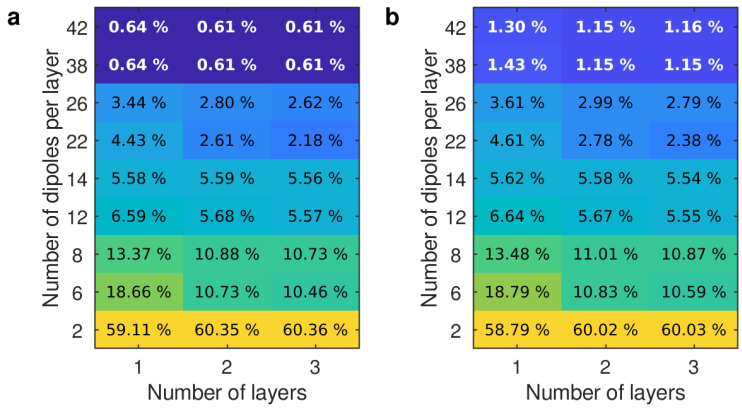

Figure 4: *Errors due to coil model simplification and fast numerical integration of secondary magnetic fields: a) test coils with accurate β integrals; b) test coils with fast numerical β integrals. The values printed in white are less than twice the error of the fast numerical approximation of β integrals.*

Table 3: *Computation speed with different coil models and implementations, presented as coil positions per second. The computations for the whole brain had $N^{\mathrm{b}} = 20324$ field points and those for regions of interest on average $N^{\mathrm{b}} = 1805$ points.*

	Whole brain			ROI		
N^{c}	76	38	14	76	38	14
Matlab (CPU)	9.4	10.6	11.5	14.0	15.0	15.5
C (CPU)	13.2	13.6	13.9	107.5	116.6	123.1
Matlab (CPU+GPU)	58.8	83.8	84.4	69.7	111	144

3.3 Speed tests

We carried out speed testing for the 38- and 14-dipole single-layer coils and the 76-dipole two-layer coil, computing the normal component of E-field for the same 251 coil locations as in the coil comparisons. Results, presented as coil positions per second (cps), are presented in Table 3. With the 38-dipole coil, we were able to compute the E field on all 20324 points of the cortex model at the speed of 83.8 cps. Computing all three field components takes about three times as long (for example, full E-field in the whole brain 27.9 and 22.8 cps for 38- and 76-dipole coils in Matlab with GPU acceleration).

4 Discussion

In this paper, we presented computational methodology for computing TMS-induced E-field in the brain in real time. The real-time performance is reached with the help of 1) an approximated solution of the integral used for computing the contribution of head conductivity on E-field and 2) a new moment-based approach for approximating the TMS coil model.

We verified and demonstrated the methods using a realistic four-compartment (4-C) volume conductor model (VCM) that contains the brain tissue, cerebrospinal fluid, skull, and scalp. For a model that in a standard PC solves one component of the E-field with 3-mm spacing on the whole cortical surface at the speed of 59 coil positions per second (cps) and in a 6-cm-radius ROI at over 100 cps, the relative error due to the the approximations was altogether 1.15%, while the difference between the 4-C and a three-shell (3-S) model that omits the cerebrospinal fluid was 29%. The computation speed in the 4-C model is clearly adequate for experimental TMS navigation use, and the error due to the introduced approximations is negligible compared to the difference between the high-detail and low-detail models.

4.1 Reciprocal approach

Our computational approach is based on the principle of reciprocity and computing the secondary electric field by weighted surface integration of discretized boundary potentials ϕ, while typical high-detail E-field models apply direct approach and volume discretization. The presented methodology does not depend on the way how the ϕ is solved—even though we used a boundary-element method [19], one can also use finite-element or finite-difference methods.

The main benefit of the reciprocal approach, partially enabling the high computation speed, is that the computations specific to each coil position can be efficiently separated from those that characterize the overall volume-conductor behavior (ϕ in Eq. 5). Related to that, the density of the mesh, where the E-field is computed, is independent of the discretization of the volume conductor model. Thus, the density of E-field sampling and thus the speed of computation can be easily varied—for example, we could apply a coarse mesh in the first stages of navigation, and change to a more detailed one in later stages of navigation that demand higher sampling or more accurate visualization. A further benefit is that the computation is done directly in terms of electric field instead of computing first the potential and then obtaining the (secondary) field via numerical differentiation over elements, as is typically done with direct approaches.

The key limitation is that the Geselowitz surface integral equation, Eq. 3, is valid only for isotropic medium; thus, the anisotropic conductivity of white matter cannot properly be accounted for. According to FEM simulations [21], the anisotrophy has a very small effect on E-field amplitude in gray matter, but in white matter the effect is on average 7%

(max. 40%). Thus, if one aims to model the E-field in white matter, imaging data needed for modeling the anisotrophy is available, and real-time performance is not required, one might want to choose the direct approach and FEM modeling instead of the reciprocal approach as used here.

The main challenge in implementing the reciprocal approach is that we need to place dipoles in all field points, and placing dipoles too close to conductivity boundaries may lead to numerical problems; the approach is thus best suited for computing field on a surface in the brain instead of volume grids that extend across many conductivity regions. In the simulations of this work, the field space was spanned at the boundary of gray and white matter, at least 1.5 mm from the pial boundary, and the density of the pial mesh was 4 mm; these parameters have been shown to be safe for the MEG problem [20] that is numerically more challenging due to its use of smaller coils.

4.2 Coil model

We used Magstim 70 mm figure-of-8 coil as our example coil and modeled it following the specifications reported in [14]. A real-world coil has spiral windings, but we modelled the coil windings as a system of circular loops. This common simplification, used e.g. in [14, 2, 21, 6, 9] enables the use of analytically-computed reference moments, facilitating our method development considerably by removing one degree of numerical uncertainty. We solved also the dipole radii and weights analytically. Our dipole placement rules in Table 2 were derived for a system of circular disks, so they hold for all planar coils with circular loops; the radii of dipole wings and weights of dipoles will need to be fitted separately for different windings.

The optimization of our dipole placements is based purely on geometrical moments. This approach does not guarantee optimal approximation of the E-field, but as our simulations show, the moment-optimized coils perform very well in realistic field computations[2]. The independency of the coil model parameters of E-field models should also increase the robustness of the coil model. The moment approach can be generalized to non-planar and non-circular coils, but then one likely needs to resort to numerical computation of moments and thus has to pay attention to the numerical stability, especially in solving the weight equations. An alternative to numerical moment computation would be the combination of moments based on circular rings, geometrical morphing, and further optimization using E-field models.

Our 85288-dipole reference coil model was verified by comparing the magnetic vector potential $\vec{A}$ produced by it to an $\vec{A}$ computed analytically in a line-segment model of the same coil (constructed independently). This comparison is equivalent to comparing primary electric fields. In the line-segment model, each circular loop was presented using 200 straight line segments (not split to dipoles), and the wire height and thickness were

[2]With the direct approach, one may, however, need a higher-order model with higher number of dipoles, because the field produced by a sparse set of dipoles may not be sufficiently smooth in the elements nearest to the dipoles.

taken into account by dividing the cross-section of the wire evenly into 28 elements, each represented by one wire. For a coil above the primary motor cortex and field computed on the cortex, the difference (maxRE) between our reference coil and the line-segment coil was <0.006%. We also verified that our coils and algorithms produce the same primary E-field using both reciprocal and direct approaches.

The TK coil model with 2712 dipoles had a relatively large $\mathrm{maxRE}_{\mathrm{rms}}$ of 4.3%. The reason for this is the weighting rule that leads to too large weights for dipoles positioned within wire loops: in the model description [14], those dipoles were given the full weight of the loop in question, although they should get only part of that weight (see the dipole moment density f and the dipole values of our reference coil in Figure 3). Using dipole locations of the TK model and our weighting rule, we built a corrected TK model (TKc) that had the $\mathrm{maxRE}_{\mathrm{rms}}$ of 0.1%—a value expected of a coil with such a large number of dipoles.

4.3 Computation speed

With the coil models and integrals presented in this work, we can in a standard desktop PC solve one component of E field in over 100 coil positions per second (cps) in a 6-cm-radius region of interest. Equipping the computer with consumer-level graphics card enables computation on the whole cortex at the speed of over 80 cps. This speed is certainly adequate for experimental navigation use, leaving a lot of room for visualization and user interface.

The whole-brain computation is dominated by the big matrix–vector multiplication $\mathbf{d}\boldsymbol{\Phi}$. In CPU-only computations, the C program was somewhat faster than the Matlab one. The GPU implementation of $\mathbf{d}\boldsymbol{\Phi}$ speeded the Matlab computations up by a factor of six. Assuming the same GPU libraries, a C+GPU implementation would likely run only marginally faster than the Matlab+GPU implementation, the benefit coming from faster building of arrays $\mathbf{d}$ and $\mathbf{B}^{\mathrm{p}}$.

When computing in a ROI, the C version performed about six times as fast as in the whole brain, while the Matlab CPU and CPU+GPU programs got performance gains of only 40–50% and 18–30%, respectively. The main reason for this difference lies in the implementation of matrix–vector computation: Both CPU and GPU libraries used by Matlab slow down considerably when they operate on only part of the columns of $\boldsymbol{\Phi}$. Also the memory consumption increased, hinting that the libraries make copies of the needed columns instead of operating directly on them. Instead of ROIs specific to each coil location, one could use larger ROIs so that the same ROI would be used for all coil positions in a larger region. In that case, the same $\boldsymbol{\Phi}$ matrix would be used for many locations, speeding up the computations. We leave further optimization and study of GPU acceleration for future research.

Here we used a 3-mm discretization of the cortex, resulting in approx. 21000 degrees of freedom (or 63000, if all field components are computed). Combined with a boundary

potential model comprising approx. 20000 nodes, the characteristic size of the system was [21000× 20000], requiring 1.68 GB with single-precision floats, or [63000×20000], 5.04 GB. Our performance results should generalize to all systems of roughly the same size. For full-brain or large-ROI real-time computations with higher detail, the memory capacity of the GPU is at the moment the limiting factor, while for smaller ROIs even our CPU-only implementation is fully adequate.

4.4 Outlook and future research

Here we have presented, verified and benchmarked new computational methods that enable real-time E-field computation in realistic head geometry that includes the gyral structure. The new methods should have impact on all TMS applications, where more accurate targeting and precise dosing of stimulation during the TMS experiment or treatment is desired.

In near future, we plan to extend our coil modeling to other coil types and to overall develop and optimize our solver implementation. Further work is also needed in generation and optimization of anatomical models and meshing. To facilitate further development in the research community, our dipole-based coil models and example Matlab routines for field computation are available from the corresponding author for academic use.

Conflicts of interest

We have received no significant financial support for this work that could have influenced the outcome of this study. We do not have any other conflicts of interest to declare either.

Acknowledgements

Computational and storage resources of Aalto University School of Science Science-IT project are acknowledged.

References

[1] A. T. Barker, R. Jalinous, and I. L. Freeston. Non-invasive magnetic stimulation of human motor cortex. *Lancet*, 1(8437):1106–1107, May 1985.

[2] A. Thielscher, A. Opitz, and M. Windhoff. Impact of the gyral geometry on the electric field induced by transcranial magnetic stimulation. *Neuroimage*, 54(1):234–243, Jan 2011.

[3] A. M. Janssen, S. M. Rampersad, F. Lucka, B. Lanfer, S. Lew, U. Aydin, C. H. Wolters, D. F. Stegeman, and T. F. Oostendorp. The influence of sulcus width on simulated electric fields induced by transcranial magnetic stimulation. *Phys Med Biol*, 58(14):4881–4896, Jul 2013.

[4] A. Bungert, A. Antunes, S. Espenhahn, and A. Thielscher. Where does TMS Stimulate the Motor Cortex? Combining Electrophysiological Measurements and Realistic Field Estimates to Reveal the Affected Cortex Position. *Cereb. Cortex*, 27(11):5083–5094, 11 2017.

[5] I. Laakso, T. Murakami, A. Hirata, and Y. Ugawa. Where and what TMS activates: Experiments and modeling. *Brain Stimul*, 11(1):166–174, 2018.

[6] J. D. Bijsterbosch, A. T. Barker, K. H. Lee, and P. W. Woodruff. Where does transcranial magnetic stimulation (TMS) stimulate? Modelling of induced field maps for some common cortical and cerebellar targets. *Med Biol Eng Comput*, 50(7):671–681, Jul 2012.

[7] A. Nummenmaa, M. Stenroos, R. J. Ilmoniemi, Y. C. Okada, M. S. Hamalainen, and T. Raij. Comparison of spherical and realistically shaped boundary element head models for transcranial magnetic stimulation navigation. *Clin Neurophysiol*, 124(10):1995–2007, Oct 2013.

[8] A. Paffi, F. Camera, F. Carducci, G. Rubino, P. Tampieri, M. Liberti, and F. Apollonio. A computational model for real-time calculation of electric field due to transcranial magnetic stimulation in clinics. *Int J Antennas Propag*, 2015, 2015.

[9] S. Makarov, G. Noetscher, T. Raij, and A. Nummenmaa. A Quasi-Static Boundary Element Approach with Fast Multipole Acceleration for High-Resolution Bioelectromagnetic Models. *IEEE Trans Biomed Eng*, Mar 2018.

[10] R. Plonsey. Capability and limitations of electrocardiography and magnetocardiography. *IEEE Trans Biomed Eng*, 19(3):239–244, May 1972.

[11] L. Heller and D. B. van Hulsteyn. Brain stimulation using electromagnetic sources: theoretical aspects. *Biophys J*, 63(1):129–138, Jul 1992.

[12] D. B. Geselowitz. On the magnetic field generated outside an inhomogeneous volume conductor by internal current sources. *IEEE Trans Mag*, 6(2):346–347, June 1970.

[13] A. S. Ferguson, X. Zhang, and G. Stroink. A complete linear discretization for calculating the magnetic field using the boundary element method. *IEEE Trans Biomed Eng*, 41(5):455–460, May 1994.

[14] A. Thielscher and T. Kammer. Linking physics with physiology in TMS: a sphere field model to determine the cortical stimulation site in TMS. *Neuroimage*, 17(3):1117–1130, Nov 2002.

[15] A. Thielscher and T. Kammer. Electric field properties of two commercial figure-8 coils in TMS: calculation of focality and efficiency. *Clin Neurophysiol*, 115(7):1697–1708, Jul 2004.

[16] J. Mengelkamp, M. Ziolkowski, K. Weise, M. Carlstedt, H. Brauer, and J. Haueisen. Permanent magnet modeling for Lorentz force evaluation. *IEEE Transactions on Magnetics*, 51(7):1–11, 2015.

[17] M. Windhoff, A. Opitz, and A. Thielscher. Electric field calculations in brain stimulation based on finite elements: an optimized processing pipeline for the generation and usage of accurate individual head models. *Hum Brain Mapp*, 34(4):923–935, Apr 2013.

[18] Q. Fang and D. A. Boas. Tetrahedral mesh generation from volumetric binary and grayscale images. In *2009 IEEE International Symposium on Biomedical Imaging: From Nano to Macro*, pages 1142–1145, June 2009.

[19] M. Stenroos and J. Sarvas. Bioelectromagnetic forward problem: isolated source approach revis(it)ed. *Phys Med Biol*, 57(11):3517–3535, Jun 2012.

[20] M. Stenroos and A. Nummenmaa. Incorporating and Compensating Cerebrospinal Fluid in Surface-Based Forward Models of Magneto- and Electroencephalography. *PLoS ONE*, 11(7):e0159595, 2016.

[21] A. Opitz, M. Windhoff, R. M. Heidemann, R. Turner, and A. Thielscher. How the brain tissue shapes the electric field induced by transcranial magnetic stimulation. *Neuroimage*, 58(3):849–859, Oct 2011.